Visakhapatnam Chapter

Proceedings of Indian Geotechnical Conference 2020
December 17-19, 2020, Andhra University, Visakhapatnam

Investigation of Instabilities in Granular Media and Their Numerical Simulation

Debayan Bhattacharya[1], Mousumi Mukherjee[2], and Amit Prashant[1*][0000-0002-0841-5951]

[1] Indian Institute of Technology Gandhinagar, Palaj, Gandhinagar 382355, Gujarat, India
[2] Indian Institute of Technology Mandi, Mandi 175005, Himachal Pradesh, India
* Corresponding author: ap@iitgn.ac.in

Abstract. The inception of instabilities in sand across different "length-scales" viz., continuum, discrete, and laboratory element tests have been highlighted in this study. With instability onset, the material behavior no longer remains "single element" in the sense of continuum mechanics, and due care is required while calibrating different constitutive relationships for use in various numerical simulations. A laboratory "element" test can instead be viewed as a boundary value problem at the instability onset. The post-instability response of a soil specimen represents the "system-response" with the evolution of inhomogeneities being primarily influenced by the boundary conditions amongst various other factors. Instability onset in drained and undrained biaxial tests have been explored by adopting the bifurcation framework with the aid of a generalized non associative elastoplastic material model. For the locally drained globally undrained scenario within a continuum numerical framework, instability onset is found to be influenced by the refinement of mesh-discretization. Signatures of rate-dependent localized behavior of sand specimens are also commented on from numerical simulations of drained biaxial tests. To address the "pathological mesh dependence" of classical continuum modelling, we resort to a micro-mechanical discrete granular framework that considers the actual particle morphology. The numerical predictions match reasonably well with the flexible boundary plane strain experiments. The inherent grain fabric arrangement is found to be the triggering mechanism behind the localized strain accumulation at multiple zones. The influence of loading boundary conditions and various signatures of local nonuniformities is also explored with the aid of image analysis in plane strain and triaxial tests.

Keywords: sand, instability, biaxial tests, localization, flexible boundaries.

1 Introduction

Laboratory element tests on soil specimens often experience nonuniform deformations in the form of excessive localized strains (shear bands), bulging, surface buckling, volume instability, and liquefaction type "solid-fluid" instability (Bardet 1990, Bigoni 2012, Mukherjee et al. 2017). The triggering mechanism behind such observations suddenly arising out of homogeneous material response can be attributed

to the loading boundary conditions - drained or undrained; flexible or rigid, inherent material imperfections, material state (relatively dense or loose) as well as the geometry of the specimen, i.e., slenderness or aspect ratio, etc. (Mukherjee 2016, Mukherjee et al. 2017, Bhattacharya and Prashant 2020). The onset of nonuniform deformations and heterogeneities marks the inception of instabilities that act as a precursor to failure in granular materials such as catastrophic landslides - Brumadinho tailings dam failure in Brazil 2019, debris flows, etc. With instability onset, the soil specimen ceases to act as a single element in the truest sense of continuum mechanics. Thus, utmost care is needed to calibrate the constitutive relationship that serves as the "holy grail" connecting the deformations and the stresses generated within any material medium.

Soils (restricting here to sands), unlike metals or fluids (liquid and gases), behave quite differently when deformed under various loading/boundary conditions. The complex material response can be attributed to their pressure-dependency, time/rate-dependence, shear-dilatancy, and very small-strain elastic response (Mitchell and Soga 2005). In this context, it is emphasized that the parameters used for calibrating material models to be used in various numerical schemes do only hold good before the instability onset point (Han and Drescher 1993). On the other hand, post-instability material behavior denotes the "system response" with the evolving instabilities and the prevailing boundary conditions. Thus, laboratory "element" tests should rather be viewed from a boundary value problem perspective. It is because soil as a material medium inherently comes with its imperfections or the disturbances (Desai 2016) embedded within it, which appear and disappear/evolve on gradual loading. Although most geotechnical engineering structures such as foundation systems, earth embankments, retaining walls, etc., experience displacements in the small deformation range, certain scenarios require proper accurate simulation(s) of the failure mechanisms involved in the system. These include modelling of landslides, debris flows (solid-fluid transition), post-liquefaction dam response, sudden (water-table) drawdown failures in earth embankments, cracks, and fractures/fissures that propagate from the bottom subgrade of the road embankments, etc. The added complexity that arises is the "particle-continuum duality paradox" (Muir Wood 2007) of granular materials viz., sands depending upon the lens under which the material behavior is examined from *micro* to *macro* scale. Strikingly, this is evident from the fact that parameters such as the internal friction (ϕ) and dilatancy (ψ_d) angles that are widely used in continuum numerical modelling have their origins (definition) at the micro-mechanical grain-scale level. Naturally, it leads to questioning the very existence of the "uniqueness of critical state" or the critical state itself, which is considered sacrosanct in the purview of classical geomechanics. Attaining a true critical state in conventional laboratory element tests seems to be a highly disillusioned aspect (Muir Wood 2012). It is engulfed by the formation of localized nonuniform deformations and shear band(s).

Various research groups have devoted longstanding efforts to understand the complex material behavior related to instability and failure in granular materials (Vardoulakis 1981, Han and Vardoulakis 1991, Yamamuro and Lade 1997, Borja 2002, Lade 2002, Alshibli et al. 2003, Desrues and Viggiani 2004, Andrade and Borja 2007, An-

do et al. 2013, Kawamoto et al. 2018). The inception of nonuniform deformations signaling the end of logical interpretation of the stress-strain behavior of soil specimens eventually gets controlled by the formation of a single shear band or multiple bands. Thus, these zones of shear strain accumulation merely represent linear feature(s) much akin to the failure wedges along a sharp plane behind earth retaining structures or slip lines below a strip footing in case of a bearing capacity problem. Attention is drawn to the fact that most geotechnical engineering problems represent the plane strain scenario. In such a case, the forces resolved on the (shear) plane along with the relative displacements, i.e., the displacement jumps (not shear strains) across that plane, become the primary point of interest. The long-term objective is to handle seamless numerical modelling of the post-bifurcation regime, and the first stepping stone towards that requires a thorough understanding of the instability onset in granular materials. The emergence of instabilities has been explored in this study across "length-scales" in sand specimens that involve continuum, discrete, and laboratory element tests (Fig. 1).

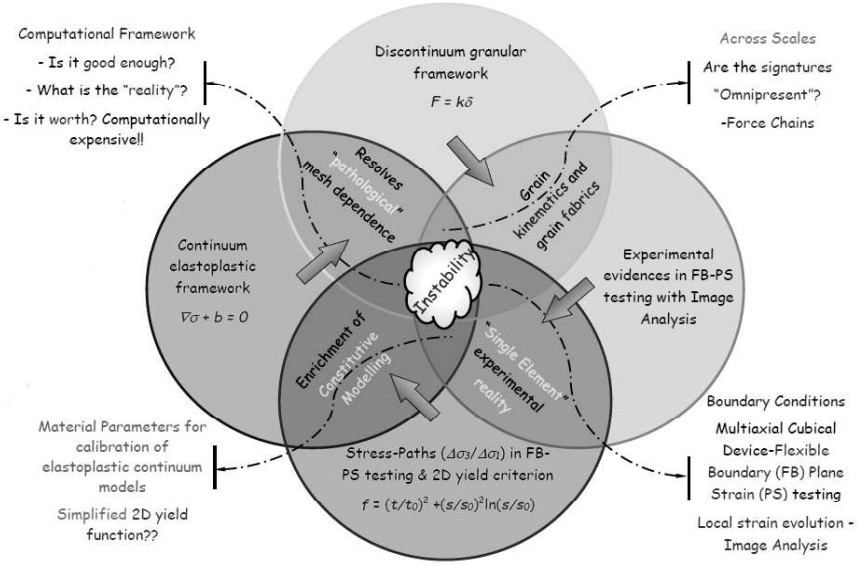

Fig. 1. Schematic illustration of the *macro-micro* interplay of instabilities in granular media (Bhattacharya 2019 - Doctoral dissertation)

Firstly, the theoretical bifurcation framework has been set up for drained and undrained biaxial tests with the aid of a generalized non associative elastoplastic material model (Gajo and Muir Wood 1999, Wood 2004). Next, the emergence of instability onset has been investigated within the realms of continuum numerical modelling. The same constitutive relationship is implemented as a user-defined material model (UMAT) within the numerical framework of ABAQUS v6.14. It explores the locally drained globally undrained scenario for a particular material state of sand and a fixed perturbation intensity. The numerical results indicate that instability onset is also a

mesh-dependent phenomenon. In order to resolve the "pathological mesh dependence" of continuum numerical modelling, material behavior is also investigated with the aid of Level Set (LS) Discrete Element Modelling (DEM) (Kawamoto et al. 2018) that takes into account the actual grain morphology, which acts as an inherent triggering mechanism behind the localized strain accumulation. The influence of loading/boundary conditions and the material response of sand specimens in Flexible Boundary (FB) Plane Strain (PS) experiments have further been explored. Signatures of nonuniform surface deformations have also been characterized for PS tests and triaxial tests with the aid of 2D digital image analysis technique.

2 Theoretical Bifurcation Framework For Instability Onset: Biaxial Drained And Undrained Element Tests

A brief mathematical formulation for plane strain bifurcation analysis of a saturated soil sample has been presented in this section, along with theoretical predictions on the possible emergence of various drained and undrained instability modes when subjected to biaxial loading conditions. With continued loading, an inhomogeneous stress-strain field may emanate from the initially homogeneous stress-strain field due to bifurcation while satisfying the same equilibrium and boundary conditions. The bifurcation analysis aims to identify a non-trivial perturbed solution, representing the difference between the inhomogeneous and homogeneous velocity fields (Vardoulakis 1981, 1985, Bardet 1991, Bardet and Shiv 1995). An existing critical-state-based nonassociative constitutive model (Gajo and Muir Wood 1999, Wood 2004), which aptly incorporates the effect of both density and confining pressure through shear and volumetric hardening, has been employed in this study for mimicking the homogeneous stress-strain field. The incremental elastoplastic stress-strain relation can be written as follows

$$\overset{\nabla}{\tau}'_{ij} = C_{ijkl} D_{kl} \tag{1}$$

where $\overset{\nabla}{\tau}'_{ij}$ is the Jaumann rate of effective Kirchhoff stress, D_{kl} is the rate of deformation tensor, and C_{ijkl} is a fourth-order tensor representing the elastoplastic tangent stiffness of the material. The instability onset in Hostun RF sand has been explored here, and the details of the associated material parameters can be found in Mukherjee (2016).

2.1 Governing equations and boundary conditions

Adopting the deformed configuration as the present configuration and in absence of body force and shear stress ($\sigma_{12} = \sigma_{21} = 0$), the stress rate equilibrium equations for a saturated soil mass under undrained biaxial condition is given as

$$\overset{\nabla}{\sigma}'_{11,1} + \overset{\nabla}{\sigma}'_{21,1} - (\sigma'_{11} - \sigma'_{22})W_{12,2} = \dot{p}_{,1}, \overset{\nabla}{\sigma}'_{12,1} + \overset{\nabla}{\sigma}'_{22,2} - (\sigma'_{11} - \sigma'_{22})W_{12,2} = \dot{p}_{,2}, \overset{\nabla}{\sigma}'_{11,1} + \overset{\nabla}{\sigma}'_{21,1} - (\sigma'_{11} - \sigma'_{22})W_{12,2} = \dot{p}_{,1}, \overset{\nabla}{\sigma}'_{12,1} + \overset{\nabla}{\sigma}'_{22,2} - (\sigma'_{11} - \sigma'_{22})W_{12,2} = \dot{p}_{,2}, \tag{2}$$

where, $\boldsymbol{\sigma}'$ is the effective Cauchy stress, W is the spin tensor, and $p$is the pore pressure. Stresses in tension and dilation have been considered to be positive. For an incompressible pore fluid, the continuity equation is as follows

$$p_{,11} + p_{,22} = b\left(v_{1,1} + v_{2,2}\right), \tag{3}$$

where, v is velocity, $b = \frac{\gamma_w}{\kappa_h}$, γ_w and κ_h are the fluid unit weight and hydraulic permeability, respectively. The rate equations for the drained condition can also be represented by Eq. (2) with $p = 0$. Fig. 2 depicts the biaxial specimen's domain geometry along with the boundary conditions to be satisfied by the perturbed velocity fields. Two types of boundary conditions have been explored, i.e., rigid lateral boundary and flexible lateral boundary. In the case of a rigid lateral boundary, the sample is subjected to constant velocities in both x_1 and x_2 direction at the boundaries $x_1 = \pm L_1$ and$x_2 = \pm L_2$, respectively. Instead, for the flexible lateral boundary, the top and bottom boundary ($x_2 = \pm L_2$) of the soil sample are given constant velocity in x_2 direction and the lateral surfaces are subjected to constant σ_{11}. The stress boundary conditions are imposed in terms of the nominal stress rate ($\dot{S}$). An additional boundary condition, i.e., no fluid flow across the boundaries, must be satisfied for the undrained case.

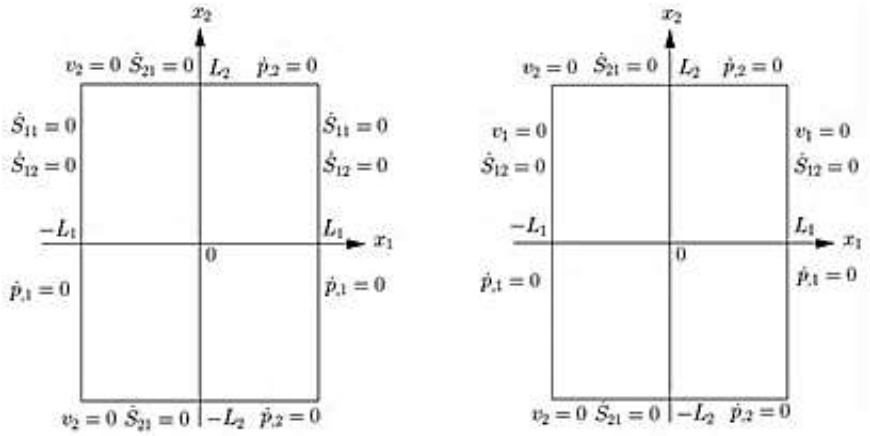

Fig.2. Boundary conditions for plane strain bifurcation with (a) flexible and (b) rigid boundary conditions under undrained loading.

2.2 Perturbed velocity fields associated with various instability modes

Undrained solid-fluid instability. The general expression for perturbed velocity field associated with solid-fluid (SF) instability can be given as

$$v_1 = V_1 \sin(\gamma_1 x_1 + \theta_1)\cos(\beta_2 x_2 + \theta_2) f(t)$$
$$v_2 = V_2 \cos(\gamma_1 x_1 + \theta_1)\sin(\beta_2 x_2 + \theta_2) f(t)$$
$$\dot{p} = P \cos(\beta_1 x_1 + \theta_1)\cos(\beta_2 x_2 + \theta_2) f(t), \quad (4)$$

where V_1, V_2, P are the arbitrary modal amplitudes, $f(t)$ is an unknown function of time. The coefficients β_1, β_2, γ_1, θ_1, θ_2 are chosen such that the perturbed velocity modes satisfy the respective boundary conditions. Eq. (4) along with Eq. (2) and (3) yield the condition for SF instability. Following is the condition for an infinite growth of SF instability under flexible lateral boundary

$$\bar{G} = (d_4 + d_7)\gamma_1^2\beta_2^2 - \beta_2^2(d_1\gamma_1^2 + d_3\beta_2^2) + \frac{l_2}{l_1}\frac{l_3}{l_4}\{(d_4 + d_8)\gamma_1\beta_1\beta_2^2 - (d_5\gamma_1^2 + d_2\beta_2^2)\gamma_1\beta_1\} = 0 \quad (5)$$

where,

$l_1 = \sin(\gamma_1 x_1 + \theta_1)$, $l_2 = \cos(\gamma_1 x_1 + \theta_1)$, $l_3 = \sin(\beta_1 x_1 + \theta_1)$, $l_4 = \cos(\beta_1 x_1 + \theta_1)$,

$d_1 = C_{1111} - \sigma_{11}$, $d_2 = C_{2222} - \sigma_{22}$, $d_7 = C_{1122}$, $d_8 = C_{2211}$, $d_3 = C_{1212} - \frac{(\sigma_{11} - \sigma_{22})}{2}$,

$d_4 = C_{1212} - \frac{(\sigma_{11} + \sigma_{22})}{2}$, $d_5 = C_{1212} + \frac{(\sigma_{11} - \sigma_{22})}{2}$, $d_6 = C_{1212} + \frac{(\sigma_{11} + \sigma_{22})}{2}$.

Equation (5) is defined within the domain $-L_1 \le x_1 \le L_1$ except at $x_1 = 0$, near which Eq. (5) can be evaluated by $\bar{G}_{0+} = \lim_{x_1 \to 0} \bar{G}$. Further, in the case of a fundamental mode, the condition reduces to the following

$$\bar{G}_{0+} = \lim_{x_1 \to 0} \bar{G} = (2d_4 + d_7 + d_8 - d_1 - d_2)\gamma_1^2\beta_2^2 - d_3\beta_2^4 - d_5\gamma_1^4. \quad (6)$$

The perturbed velocity field and the condition of emergence for SF instability under the rigid boundary case can be retrieved from Eq. (4) and (5) when $\gamma_1 = \beta_1$ is enforced (Mukherjee et al. 2017) along with the boundary condition of Fig. 2(b).

Drained diffused mode. The following expression is usually adopted for representing the drained diffused mode.

$$v_1(x_1, x_2) = V_1(x_1)\cos(\beta x_2 + \theta_2)$$
$$v_2(x_1, x_2) = V_2(x_1)\sin(\beta x_2 + \theta_2) \quad (7)$$

The coefficients β and θ_2 are selected in such a way that the velocity fields satisfy the boundary conditions, as shown in Fig. 2. A general form of velocity solution with $V_1(x_1) = Ae^{i\alpha x_1}$ and $V_2(x_1) = Be^{i\alpha x_1}$ can be substituted in the equilibrium equation leading to the following characteristic equation (Bardet 1991)

$$a_1 Z^4 + b_1 Z^2 + c_1 = 0, \quad (8)$$

where $a_1 = d_1 d_5$, $b_1 = d_1 d_2 + d_3 d_5 - (d_4 + d_7)(d_4 + d_8)$, $c_1 = d_2 d_3$, $Z = \frac{\alpha}{\beta}$.

Depending on the magnitudes of a_1, $b_1$and c_1, Eq. (8) results into four different types of solution in Z, elliptic imaginary, elliptic complex, parabolic, and hyperbolic. In this study, elliptic complex type drained diffused modes are examined for flexible lateral boundary case; whereas, rigid lateral boundaries can only result in hyperbolic solu-

tions due to the imposed boundary constraint. In a hyperbolic regime further, these modes remain in competition with the localized modes.

Localization mode. Shear bands with a zone of localized strain is another possible instability mode, which requires to satisfy the condition of velocity continuity (Rice 1976), $[v_{i,j}] = g_i n_j$. Here [.] denotes the jump in the field variable within and outside the band, ***g*** is an arbitrary vector, and ***n*** is normal to the band. The velocity continuity along with stress equilibrium across the band leads to the same characteristic equation as in Eq. (8). Two unique real solutions for ***n*** are obtained on the elliptic/hyperbolic boundary, from which the shear band angle (θ_s) can be calculated ($n_1 = \sin\theta_s, n_2 = \cos\theta_s$). The localization modes remain independent of the type of lateral boundary condition imposed during the bifurcation analysis. A locally drained condition has been assumed near the localization zone for bifurcation analysis under undrained conditions, where the coefficients of Eq. (8) are calculated based on the effective stress parameters.

2.3 Observations from bifurcation-based instability analysis

The homogeneous stress-strain field has been simulated first by subjecting the specimen to the undrained and drained biaxial loading with varying initial effective confining pressure (100-400 kPa) and initial void ratio (e_0 = 0.8-0.6). Such homogeneous stress-strain fields are then used to identify the possible onset of various instability modes by checking against the conditions mentioned in Eq. (5), (6), and (8).

Figure 3(a) depicts the initiation of solid-fluid (SF) and localization type instability modes under rigid and flexible conditions. It is interesting to obverse that SF instability emerges first just before the peak stress in loose sand for the rigid lateral boundary case, which then gets followed by the localized mode; whereas, localization precedes the SF modes for the flexible boundary case. Both SF instability and localization have been noticed to get delayed with an increase in the confinement. In the case of medium dense sand (e_0 = 0.7), only localization type of instability has been captured under flexible lateral boundary; on the contrary, the nature of first instability mode changes localization to SF instability with a decrease in the confinement under rigid lateral boundary condition.

The drained diffused antisymmetric modes emerge only for the cases with a flexible lateral boundary condition at higher initial confinement and in slender specimens, e.g. $\frac{L_2}{L_1} \geq 3$ (Fig. 3b); however, once activated it nearly remains independent of the confining pressure. Unlike diffused modes, localization is observed to initiate at all the confinement levels, and further, localization onset gets retarded with an increase in the initial confining pressure. Reduction in the magnitude of shear modulus ($\mu = \frac{G_0}{6}$) further delays down the localization onset as depicted in Fig. 3(c). Also, the diffused antisymmetric modes now start to emerge even at lower confinements and for specimens with a lower aspect ratio ($\frac{L_2}{L_1} = 2$). With the further reduction of shear modulus ($\mu = \frac{G_0}{9}$), the symmetric diffused modes start to appear in bulky specimens

($\frac{L_2}{L_1} = 1$) of denser sand at very high confinement (Fig. 3d). It should be noted that such drained diffused instability modes are only possible to capture within a large deformation-based formulation with due consideration to the geometric nonlinearity (Mukherjee et al. 2016). Further, compared to the large deformation formulation, a small deformation framework overpredicts both the onset strain of localization and the band inclination angle.

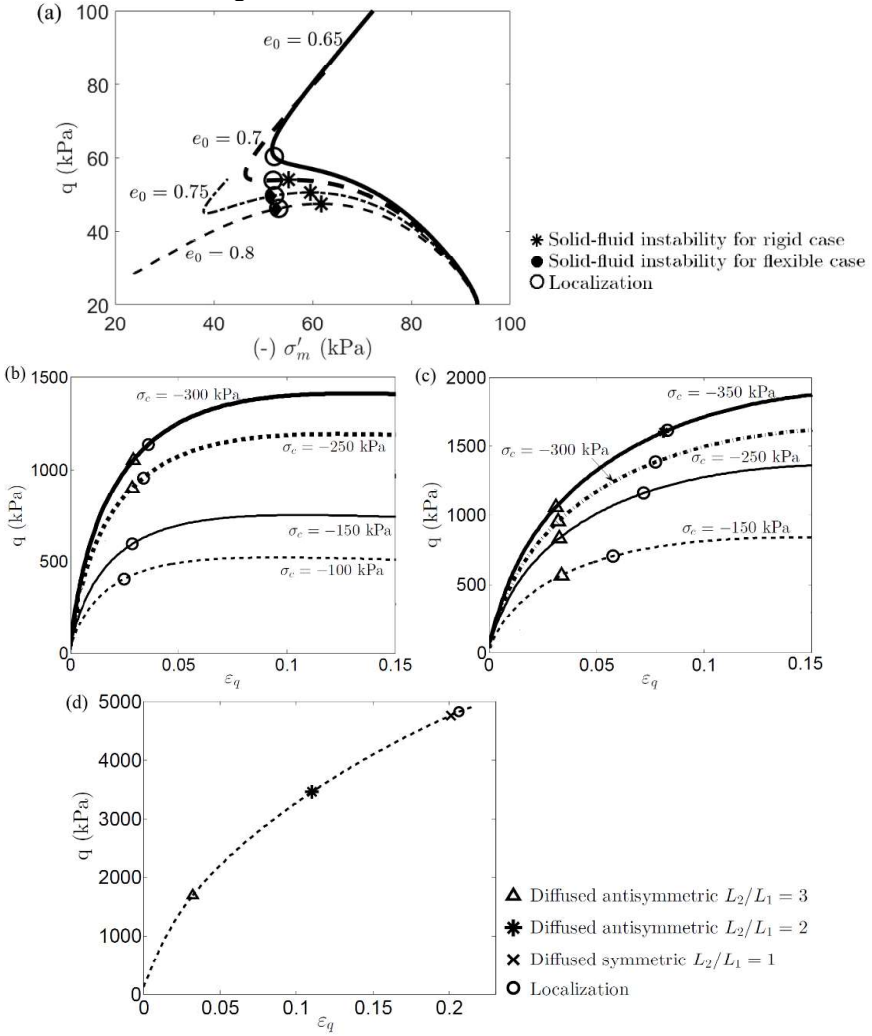

Fig. 3. (a) Stress-paths and initiation of undrained instabilities at σ_c' = -100 kPa for varying e_0, (b, c) Stress-strain and emergence of various drained instabilities with varying confinement at e_0 = 0.75 for two values of shear modulus, $\mu = G_0/3$ and $\mu = G_0/6$, respectively, (d) initiation of various drained instabilities at e_0 = 0.7 for σ_c' = -600 kPa with $\mu = G_0/8$, where G_0 is the small strain shear modulus

3 Exploring Instability Onset Within A Numerical Framework: Mesh-Dependent Issues

This section is on the instability onset in Hostun RF sand specimens within the continuum numerical framework of ABAQUS v6.14 by using UMAT for the state-dependent constitutive relationship (Gajo and Muir Wood 1999, Wood 2004). In order to trigger instability, material inhomogeneity has been introduced in terms of a generic parameter - initial void ratio (e_0) unlike other studies (Shuttle and Smith 1988, Borja and Regueiro 2001), since instability onset will essentially become a material model-dependent phenomenon in that case.

3.1 Locally drained globally undrained biaxial test simulations

First, locally drained globally undrained (transient analysis, i.e., coupled with diffusion) numerical simulations were carried out on square biaxial specimens of 100 mm side length with a fixed perturbation intensity introduced in terms of e_0. Dense configuration (e_0 = 0.6) was considered for all the simulations. A mesh convergence study is carried out with a paltry amount of perturbation (P) = 0.01% e_0 introduced within the system (in the middle element) to match the theoretical predictions reported from bifurcation analysis by Mukherjee et al. (2017). The drop or the deviation in the force (F) displacement (δ) relationship demarcates the instability onset point. For relatively lesser elements, the material response is uniform and homogeneous (Fig. 4a) while, with gradual mesh refinement, the axial strain at instability onset (ε_a^b) reduces significantly. ε_a^b reduces to almost 1.8% for 400 elements from a uniform response as exhibited for specimens with fewer elements. Interestingly, ε_a^b reduces down gradually tracing out the same F-δ curve denoting that instability onset in undrained conditions is also a mesh-dependent phenomenon. F-δ response for different P also highlights that ε_a^b gets significantly influenced as the magnitude of P is increased (Fig. 4b).

These aspects can be found in more detail elsewhere (Bhattacharya et al. 2020*a*). A particular case of the dense sand specimen with P = 0.1% e_0 is examined here in more detail, and Fig. 4c represents the local shear strain contour at instability onset with elements marked inside and outside the localized zone of strain accumulation. On a closer look at the local (elemental-E) shear stress (q) vs. shear strain (ε_q) plot (Fig. 4d), the stress drop can be seen for those elements within the pervasive shear band (E 210 and 235) zone, while the one far away from the localized zone (E 377) displays a nearly uniform stress-strain response. It is emphasized that perturbation was introduced in the middle element, which acts as the localization attractor in this case. The (local) fluid velocity vectors at the beginning and instability onset are shown in Fig. 4e and 4f, respectively. At instability onset, all the fluid velocity vectors align themselves in a preferred direction towards the weak element (middle of the specimen). The shear strain contour plot (Fig. 4c) also demarcates the contractive zones adjacent to the (dilative) localized zone. It emphasizes the important consideration of the local fluid motion in a globally undrained scenario. These observations are in line with

those reported by Han and Vardoulakis (1991) from radiographic studies on fluid-saturated sand specimens.

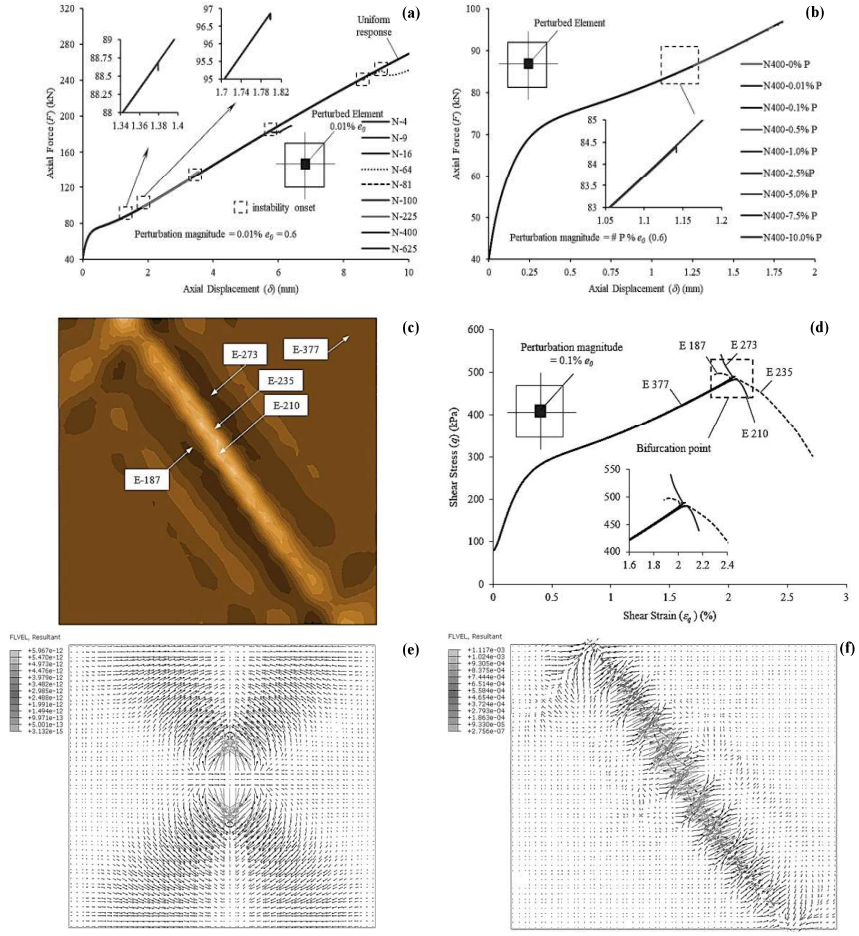

Fig. 4. Locally drained globally undrained biaxial simulations: (a) axial force (F) vs axial displacement (δ) for different mesh discretization and perturbation intensity $P = 0.01\%\ e_0\,(0.6)$ (b) F-δ response for different perturbation intensity (with $N = 400$ elements) (c) shear strain contour (ε_q) at instability onset with element positions ($P = 0.1\%\ e_0$) (d) local shear stress (q) vs local shear strain (ε_q) at instability onset ($P = 0.1\%\ e_0$) and fluid velocity vectors (in m/sec) at the (e) start of simulation (f) instability onset

3.2 Rate-dependent localized behavior of sand in drained biaxial tests

Mukherjee et al. (2020) extended the rate-independent constitutive model of Wood (2004) to a rate-dependent form by coalescing it with a Perzyna (1963) type over-stress framework. The model has further been employed in ABAQUS by writing UMAT subroutine, and the influence of strain-rate on localization behavior of Hostun-RF sand has been explored for a drained biaxial simulation. A perturbation in the form of local heterogeneity has been induced by altering the magnitude (0.5% less than the global value) of one of the state variables, i.e., initial stress ratio at the corner most element. Instead of the global force-displacement approach, local variations in shear strain response have been noticed to be more effective in identifying the bifurcation onset within a numerical framework.

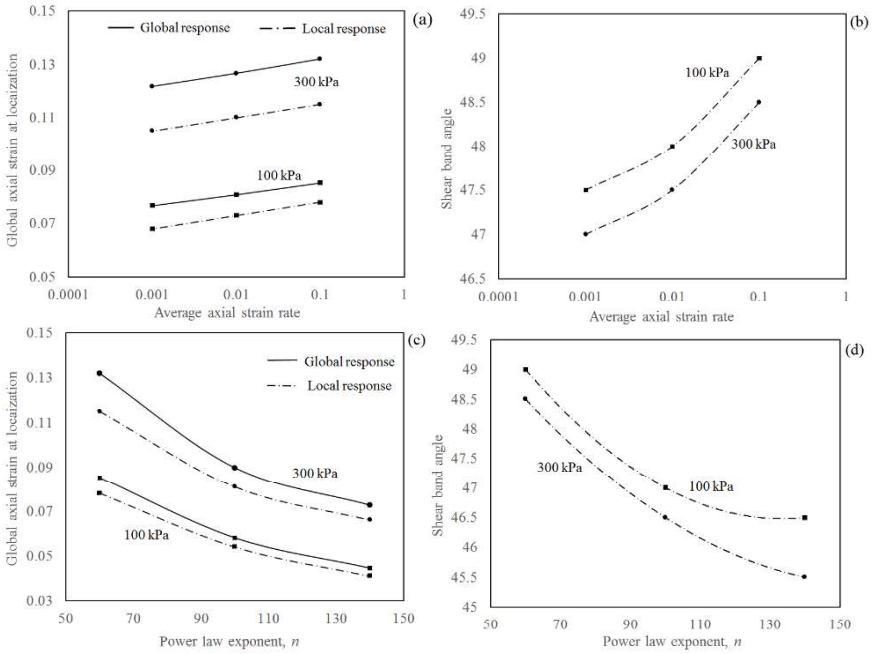

Fig. 5. Variation in (a, c) global axial strain at localization (considering both global and local response) and (b, d) shear band angle with strain rate and power-law exponent, n, respectively at two initial confining pressures for $e_0 = 0.9$.

Once the mesh convergence has been achieved, the thickness of the shear band remains independent of the mesh size due to the underlying rate-dependent model, which regularizes the localization problem by inducing a length scale through the presence of an inherent time scale (Needleman 1988). The variation of localization onset and shear band inclination at three different strain rates have been plotted in Fig. 5(a, b). An increase in strain rate delays the localization onset, which is generally noticed to initiate in the hardening regime in loose sand. Similar to the rate-

independent case, an increase in confinement further retards the localization onset. Shear band angle (measured anticlockwise from horizontal) also increases with an increase in the applied strain rate, e.g., at e_0= 0.79 and 100 kPa initial confinement, the band angle increases from 47.5° to 49° as the strain rate increases from 0.001 to 0.1 /sec. It is interesting to note that the predicted shear band angle, from a bifurcation-based rate-independent instability analysis, for this case is 47.6°. Unlike the band angle, the shear band thickness has been noticed to remain independent of the strain rate. The effect of rate-sensitivity of the material on localization behavior has further been studied by altering one of the material parameters, strain rate exponent *n*. Similar to higher rates, a lower value of *n*, i.e., higher rate-sensitivity, delays the emergence of localization and leads to an increase in the shear band angle (Fig. 5c, d).

4 Seeing The Granular World: Micromechanical Origins of Instability Onset And Its Evolution In Biaxial Tests

Unlike the continuum numerical framework that requires the heterogeneities (perturbation) to be introduced within the material domain to trigger instability onset, nonuniform deformations in a discrete granular setting manifest themselves due to their inherent grain imperfections and the particulate (fabric) arrangement. The grain-scale kinematics and the underlying governing physics of the localized strain accumulation are explored in great detail with the aid of LS-DEM (Kawamoto et al. 2018) which takes into account the actual particle morphology. Level-Sets (mathematical descriptors) of representative sand grains (Grade II Ennore sand-subangular to angular; 0.5-1 mm) with nodes seeded on the particle boundary are acquired (Fig. 6a) from which the dense particle assembly is generated (Fig. 6b) by following a random distribution. Flexible Boundary (FB) 2D-Plane Strain (PS) simulations are carried out in this study.

The FBs are modelled using circles that are connected to each other with springs, and they interact with the sand grains on progressive loading. The nodes seeded on the grain boundaries are used for determining the particle penetration and grain contact(s). A classical Coulomb type friction model is considered for the sand grains, and they are modelled using both normal and tangential stiffness. The particulate modelling details can be found elsewhere (Kawamoto et al. 2018, Bhattacharya et al. 2020*b*). It is pertinent that FBs resemble the boundary conditions in the field scenario, which justifies adopting them in the present context. First, the soil specimen is consolidated along both the axes. Once a negligible volume change is recorded, the specimen is sheared by deforming it vertically while a constant pressure (50 kPa) is maintained along the horizontal axis. The global material response is matched against the FB-PS experiments that are carried out in a newly developed multiaxial test setup (Bhattacharya and Prashant 2020). The onset of localized strain accumulation is captured at small strains (2% of global axial strain ε_a) from a few grains within the specimen (encircled in Fig. 6c). The local shear strain is plotted on the discrete grains itself following a Delaunay triangulation (for neighborhood grain networks) and Cundall's best-fit strain formulation (Bagi 2006).

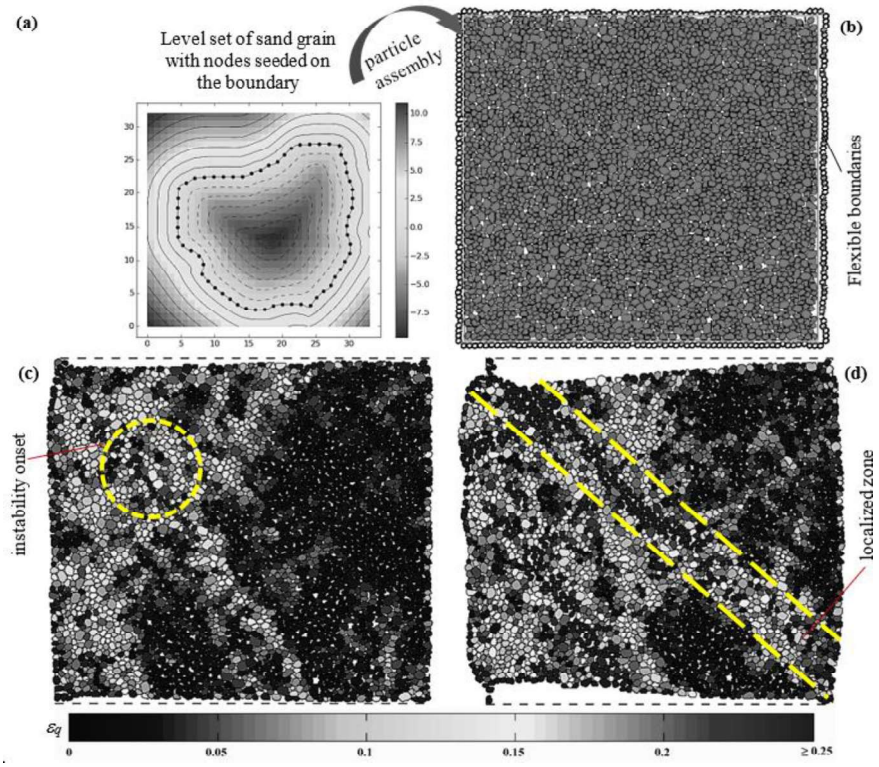

Fig. 6. Discrete granular framework exploring instability in biaxial tests: (a) level-set of single sand grain with nodes seeds on the particle boundary (b) dense particle assembly/configuration with flexible boundaries and local shear strain (ε_q) distribution of the assembly in between (c) 0-2% global axial strain (ε_a) and (d) 4-6% ε_a

Further biaxial shearing results in a distinct zone of intensive straining (Fig. 6d) in between 4-6% ε_a. Interestingly, the shear band is followed by multiple zones of strain-accumulation throughout the specimen. These zones appear and disappear (evolve) on progressive deformation. The force chains become weak in these regions while the transmission paths evolve as the granular specimen is being loaded. A closer look at the particle rotations also reveals that the grains undergo significant rotation within these localized zones while they orient themselves (fabric) along a preferred loading direction. Thus, the inherent particle morphology and the grain arrangement trigger nonuniform deformation(s) in the sand specimen. Unlike the continuum numerical modelling where the material response can be reasonably captured until instability onset and very little can be commented on the post-instability response (mesh-dependence issues), the discrete micromechanical framework seamlessly allows capturing the "system response" along with the evolving instabilities.

5 Influence of Loading Boundary Conditions On Material Response And Estimation of Local Nonuniformities: Experimental Evidence With 2D Image Analysis

The loading/boundary conditions can significantly influence the material response observed in laboratory element tests. Consequently, they affect the onset of nonuniform deformations, and eventually, its evolution is registered as "system-response" rather than inherent material behavior. FB-PS tests have been performed on dense (dry densityρ_d = 1.8 gm/cc) cubical sand specimens of side length 96 mm in the multiaxial testing device (Fig. 7a) that was developed *in-house* (Bhattacharya 2019). The transparent rigid plexiglass boundaries impose the PS constraints (ε_z = 0) and allow images to be taken during shearing. The experimental setup comprises pressure housings with LVDTs attached in each of the axes that measure the specimen deformation and are in contact with the FBs (made of butyl rubber) surrounding the four sides (Fig. 7b). To investigate the influence of loading boundaries, the FBs along the deformation axis was slightly modified in another series of tests (mixed boundaries-MB). A relatively rigid thin aluminum sheet (0.3 mm) was fixed to the deformation-controlled boundary in front of the FBs (Fig. 7c). A more detailed discussion on the experimental front can be found elsewhere (Bhattacharya and Prashant 2020).

The images taken during the shearing stage are analyzed using the 2D-Digitial Image Correlation technique (GeoPIV-RG: Stanier et al. 2015). The surface deformations on the PS boundary present two different pictures for the two types of PS tests with FBs and MBs. The displacement vectors for the MB-PS test (Fig. 7e) indicate that the particle (sand grains) flow had a preferential bias (local heterogeneities) towards the lateral (flexible) boundaries from the initial stages (2% ε_a) of the test itself. In contrast, the FB-PS test exhibited relatively uniform deformations at the beginning (Fig. 7d). However, local nonuniformities (shear strains) in the case of FB-PS test manifested from the specimen corners (Fig. 7f). Although the material response, in this case, was largely uniform, at large strains (8% ε_a) significant non-uniformities (with a difference in gradients) were registered mostly concentrated at the specimen corners (Fig. 7g). The MB-PS test deviated from the actual material behavior, and the non-uniformities in the displacement field was triggered as a consequence of the loading boundaries. It is important to recognize this aspect to ensure proper boundary conditions in laboratory "element" tests based on which various material models are calibrated for different numerical modelling schemes.

A further investigation was undertaken to explore the signatures of inhomogeneities emerging in conventional triaxial tests with rigid frictional and lubricated boundaries. This exercise was carried out on dense, medium dense (ρ_d = 1.66 gm/cc) and loose (ρ_d = 1.47 gm/cc) sand specimens, and the surface deformations were eventually estimated from the images that were taken during the shearing.

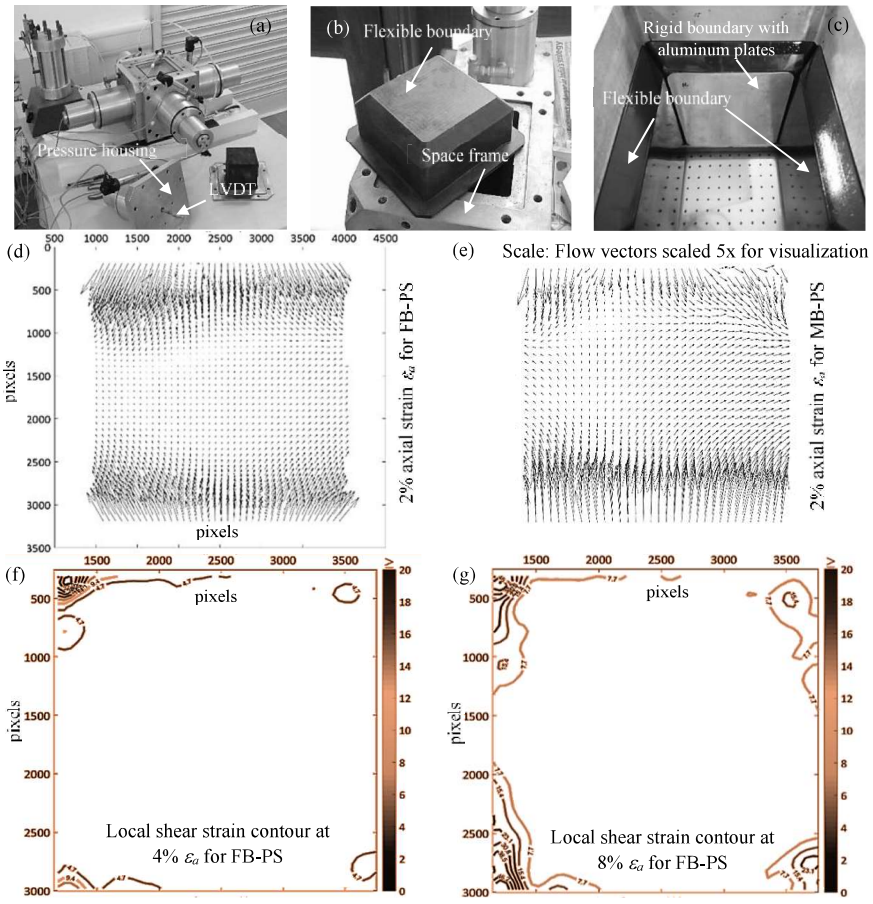

Fig. 7. Flexible Boundary (FB) Plane Strain (PS) testing: (a) experimental setup (b) flexible boundary (c) aluminum sheets attached to the FBs along the deformation-controlled axis for Mixed-Boundary (MB)-PS testing; displacement vectors at 2% axial strain ε_a for (d) FB-PS and (e) MB-PS testing; local shear strain contours for FB-PS test at (f) 4% and (g) 8% ε_a

Clearly, the initial response was nearly uniform for the dense specimen subjected to a rigid frictional base (Fig. 8a) while at large strains (8% ε_a) with progressive loading, an intense zone of straining in an X-shape could be noticed in the middle (Fig. 8b). On the other hand, instability onset for the dense specimen with lubricated ends was initiated from the right bottom corner, which became quite evident at around 3.6% ε_a (Fig. 8c). This further spread to the other corner, and eventually, distinct conjugate bands were noticed to emerge at around 12.2% ε_a (Fig. 8d). Interestingly, these kinematic features also get reflected in the global material response (measured at the boundaries), with the frictional ends exhibiting a strikingly distinct softening response, as compared to the specimen with a lubricating base. Contrary to the dense specimen, where the nonuniform deformations were primarily observed to be local-

ized in some regions, heterogeneities in case of medium dense (Fig. 8e, 8f) and loose (Fig. 8g, 8h) sand specimens subjected to frictional bases tend to emerge from the middle of the specimen. On progressive loading (at 7.8% ε_a), these inhomogeneous deformations were observed to spread throughout the sand specimens. Similar signatures were noted for medium dense and loose sand specimens with rigid lubricated bases owing to which the discussion has not been repeated.

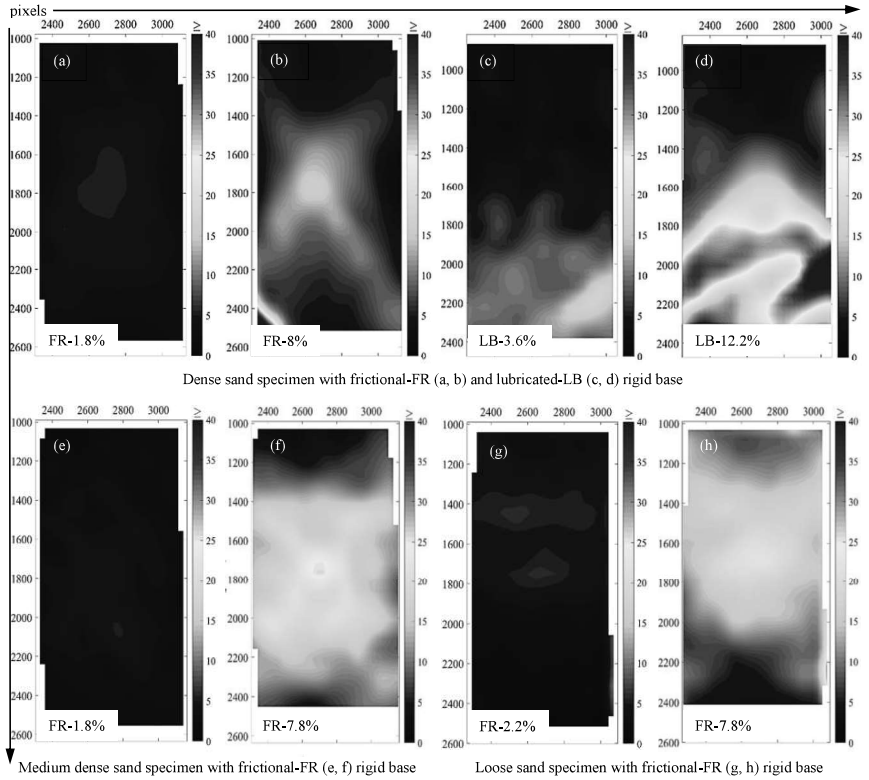

Fig. 8. Local shear strain contour plots for triaxial tests with rigid base: for dense specimen with frictional (FR) ends at (a) 1.8% (b) 8% global axial strain (ε_a); with lubricated (LB) ends at (c) 3.6% (d) 12.2% ε_a; for medium dense specimen with FR ends at (e)1.8% (f) 7.8% and for loose specimen with FR ends at (g) 2.2% and (h) 7.8%

6 The Way Forward And Concluding Remarks

Instabilities in granular media and their omnipresent features have been explored across "length-scales" in the context of plane strain scenario in this study. The way forward in geomechanics needs due consideration to instabilities and nonuniform deformations that act as a precursor to failure in various geotechnical boundary value problems e.g., slope stability failures, landslides, retaining wall failures, borehole

instabilities, etc. The multiscale modelling approaches (Andrade et al. 2011, Ai and Feng 2020, Zhao et al. 2020) have gained popularity in recent times with a gradual shift from the semi-empirical formulation to a more physics-based approach (e.g., Discrete Element Modelling, Material Point Method, Smooth Particle Hydrodynamics, Peri-dynamics, etc.). However, these numerical tools are primarily restricted to research and academia. Issues persist in the classical continuum framework, and attempts to resolve those aspects are still being made with Coupled Eulerian-Lagrangian formulation, micropolar (Cosserat), and the non-local approach, strain-gradient framework, etc. Besides the needed effort for revisiting the classical numerical framework (Yang and Misra 2012, Placidi et al. 2018), it is required to work on hybrid formulations while appraising the shortcomings of the constitutive relationships. In this regard, the disturbed state framework (Desai 2016) claims to be a promising candidate for granular materials.

Further, it is required to shift the focus of research to unravel the real truth - soils inherently pose imperfections (unlike weak brittle fractures in jointed or pristine rocks), i.e., disturbances are embedded within the system itself. Instead of focusing the attention towards a single pervasive shear band (extending up to 10-20d_{50}; d_{50} = mean grain-size diameter) in laboratory element tests, which is considered to manifest as slip line(s)/ failure wedge(s) in the field, the attempt should be devoted towards understanding the regular patterning (i.e., evolution) or kinematic features that appear and disappear on progressive loading. Naturally, this questions the very basis or the existence of the hallowed asymptotic "critical state" while the specimen may have regular patterning (very different from a single intensive zone of strain accumulation). Thus, the lens under which the soil specimen is being examined and the regular patterning may seem to be spread "*homogeneously heterogeneous*" (Muir Wood 2012) throughout the system. Consequently, these intriguing aspects seem to question our very fundamental (debatable) belief system - Do we know enough information from a laboratory size specimen ("element") to extrapolate it to an actual field problem? What (constitutive features) causes the patterning that we observe in a laboratory size specimen? What other constitutive parameters do we need to model the post-instability "system response" (with the prevailing boundary conditions) or the failures in geomaterials?

A plausible alternative is that we take recourse to the computational tools (e.g., DEM in conjunction with X-ray μCT) and investigate the laboratory "element" test as a boundary value problem. Insights gained at the particulate (*micro*-scale) level can be compared against those measured at the specimen boundaries. In this way, it can be assured that the breaks in the force-transmission paths, weak links, or slips at the grain contacts manifest themselves into the bulk material response observed experimentally (*meso*-scale). Consequently, these features can be upscaled (computationally hierarchical approach) for a reasonable volume of mass such that it represents an equivalent continuum narrative that can be reasonably applied for geotechnical structures (*macro*-scale) in the field. Although these aspects are well beyond the present-day computational know-how, nevertheless they should be duly acknowledged. The climax of these rigorous semi-analytical approaches (e.g., bifurcation analysis) and seamless computational handling of instabilities can be reached once these advance-

ments are gradually incorporated into engineering practice as an alternative to a semi-empirical framework for next-generation modelling of geomaterials in the years to come. The authors have made attempts to highlight some important features related to instabilities in granular media. The key takeaways or aspects are listed below:

1. The bifurcation-based instability analysis reveals that stress-controlled flexible boundary favors the emergence of diffused drained instability modes, initiation of which further gets enhanced with the increase in the confinement level, reduction in the material stiffness and density, and increase in the slenderness of the specimen.
2. A rigid lateral boundary is more conducive to the emergence of diffused solid-fluid instability under undrained conditions.
3. Under continued shearing, such diffused instabilities often lead to localized modes, which further mark the specimen's failure. Hence, it is imperative to understand and predict the onset of various drained and undrained diffused instabilities reasonably well.
4. Coupled undrained (locally drained globally undrained scenario) instability analysis in sand specimens reveals that instability onset within a continuum numerical framework for a particular amount of perturbation intensity is a mesh-dependent phenomenon. The conventional mesh-convergence study (required to achieve the overall material response) and that required for instability (onset) analysis are two different aspects, with the latter naturally requiring finer mesh.
5. The permeability factor introduces an inherent length-scale within the transient numerical formulation; however, it is insufficient to address the mesh-regularization aspects to achieve an objective solution.
6. The state-dependent material model reasonably captures the occurrence of adjacent dilative (shear zone) and contractive bands at the instability onset with the local fluid velocity vectors aligning themselves in a preferred direction towards the weak element (localization attractor). These features match qualitatively with the experimental findings reported in the literature.
7. Apart from mesh-regularization aspects, the material's inherent rate-sensitivity can influence the localization onset or shear band formation in soil under a high strain-rate.
8. In a discrete micromechanical setting, local nonuniformities get triggered at relatively small strains from a few grains within the (FB-PS) particulate system. The inception of heterogeneities is attributed to the inherent particle morphology and the grain fabric.
9. The sand grains in the zones of intense shearing are also accompanied by a significant amount of rotation. Further, the force chains become weak in these regions, and the transmission paths take an alternate recourse. With progressive shearing, the sand grains tend to orient themselves along the (preferred) direction of principal loading (axis).
10. PS tests on dense sand specimens with flexible and relatively rigid deformation boundaries display a different material response. Consequently, the emergence of instabilities marked with signatures of non-uniformities in the

displacement field is also largely influenced by the loading boundary conditions. A preferential bias of particle movement is observed (towards the lateral FBs) in the case of MB-PS tests even at small strains from the beginning. In contrast, in the FB-PS test, non-uniformities emerge from the specimen corners, which accumulates over the loading stage.

11. Compared to the PS scenario, triaxial tests with rigid frictional and lubricated boundaries exhibited conjugate zones of intense shear strains localized at a particular region. On the other hand, for medium dense and loose specimens (subjected to frictional ends) nonuniformities emerge from the middle and spread throughout the system on subsequent loading. It is pertinent that the constitutive relationships that are developed within the classical continuum framework are only applicable for homogeneous straining ("element" consideration), and due care needs to be ensured for calibrating the model parameters.

References

1. Alshibli, K. A., Batiste, S.N., and Sture, S.: Strain localization in sand: plane strain versus triaxial compression. Journal of Geotechnical and Geoenvironmental Engineering 129 (6), 483–494 (2003).
2. Andrade, J. E., and Borja, R.I.: Modeling deformation banding in dense and loose fluid-saturated sands. Finite Elements in Analysis and Design 43 (5), 361–383 (2007).
3. Andrade, J. E., Avila, C. F., Hall, S. A., Lenoir, N., & Viggiani, G.: Multiscale modeling and characterization of granular matter: from grain kinematics to continuum mechanics. Journal of the Mechanics and Physics of Solids, 59(2), 237-250 (2011).
4. Andò, E., Viggiani, G., Hall, S. A., & Desrues, J. Experimental micro-mechanics of granular media studied by X-ray tomography: recent results and challenges. Géotechnique Letters, 3(3), 142-146 (2013).
5. Ai, S. G., & Feng, S. J.: Multiscale modeling for analyzing slip weakening at material interfaces. Computers and Geotechnics, 118, 103348 (2020).
6. Bagi, K.: Analysis of microstructural strain tensors for granular assemblies. International Journal of Solids and Structures 43 (10), 3166-3184 (2006).
7. Bardet, J.: A comprehensive review of strain localization in elastoplastic soils. Computers and Geotechnics 10 (3), 163–188 (1990).
8. Bardet, J. P.: Analytical solutions for the plane-strain bifurcation of compressible solids. Journal of Applied Mechanics, 58, 651-657 (1991).
9. Bardet, J. P. and Shiv, A.: Plane-strain instability of saturated porous media. Journal of Engineering Mechanics, 121, 717-724 (1995).
10. Bhattacharya, D.: Instabilities in granular media with flexible boundaries. Doctoral dissertation, Indian Institute of Technology Gandhinagar, (2019).
11. Bhattacharya, D., & Prashant, A.: Effect of loading boundary conditions in plane strain mechanical response and local deformations in sand specimens. Journal of Geotechnical and Geoenvironmental Engineering, 146 (9), 04020086 (2020).
12. Bhattacharya, D., Mukherjee, M., & Prashant, A.: Perturbation intensity and mesh convergence in coupled undrained instability analysis in sands under biaxial loading. International Journal of Geomechanics, 20 (7), 04020081 (2020*a*).

13. Bhattacharya, D., Kawamoto, R., Karapiperis, K., Andrade J.E., & Prashant, A.: Mechanical behaviour of granular media in flexible boundary plane strain conditions: experiment and level-set discrete element modelling. Acta Geotechnica (2020*b*). https://doi.org/10.1007/s11440-020-00996-8
14. Bigoni, D.: Nonlinear solid mechanics: bifurcation theory and material instability. Cambridge University Press (2012).
15. Borja, R. I.: Bifurcation of elastoplastic solids to shear band mode at finite strain. Computer Methods in Applied Mechanics and Engineering 191 (46), 5287–5314 (2002).
16. Borja, R. I., and R. A. Regueiro.: Strain localization in frictional materials exhibiting displacement jumps. Computer Methods in Applied Mechanics and Engineering 190 (20-21), 2555-2580 (2001).
17. Desai, C. S.: Disturbed state concept as unified constitutive modeling approach. Journal of Rock Mechanics and Geotechnical Engineering 8 (3), 277–293 (2016).
18. Desrues, J. and Viggiani., G: Strain localization in sand: an overview of the experimental results obtained in Grenoble using stereophotogrammetry. International Journal for Numerical and Analytical Methods in Geomechanics 28 (4), 279–321 (2004).
19. Gajo, A., & Muir Wood, D.: A kinematic hardening constitutive model for sands: the multiaxial formulation. International Journal for Numerical and Analytical Methods in Geomechanics, 23(9), 925-965 (1999).
20. Han, C. and Drescher, A.: Shear bands in biaxial tests on dry coarse sand. Soils and Foundations 33 (1), 118–132 (1993).
21. Han, C. and Vardoulakis, I.: Plane-strain compression experiments on water saturated fine-grained sand. Ge′otechnique 41 (1), 49–78 (1991).
22. Lade, P. V.: Instability, shear banding, and failure in granular materials. International Journal of Solids and Structures 39 (13-14), 3337–3357 (2002).
23. Kawamoto, R., Andò, E., Viggiani, G., & Andrade, J. E..: All you need is shape: Predicting shear banding in sand with LS-DEM. Journal of the Mechanics and Physics of Solids, 111, 375-392 (2018).
24. Mitchell, J. K., & Soga, K.: Fundamentals of soil behavior (Vol. 3). John Wiley & Sons, New York (2005).
25. Muir Wood, D.: Heterogeneity and soil element testing. Ge′otechnique Letters 2, 101–106 (2012).
26. Muir Wood, D.: The magic of sands—the 20th Bjerrum Lecture presented in Oslo, 25 November 2005. Canadian Geotechnical Journal, 44(11), 1329–1350 (2007).
27. Mukherjee, M.: Instabilities and rate-dependency in mechanical behavior of sand, Doctoral dissertation, Indian Institute of Technology Kanpur, (2016).
28. Mukherjee, M., Gupta, A., and Prashant, A.: Drained instability analysis of sand under biaxial loading using a 3D material model. Computers and Geotechnics, 79, 130-145 (2016).
29. Mukherjee, M., Gupta, A., & Prashant, A.: Instability analysis of sand under undrained biaxial loading with rigid and flexible boundary. International Journal of Geomechanics, 17 (1), 04016042 (2017).
30. Mukherjee, M., Gupta, A., and Prashant, A.: A rate-dependent model for sand to predict constitutive response and instability onset. Acta Geotechnica, https://doi.org/10.1007/s11440-020-00988-8 (2020).
31. Needleman, A.: Material rate dependence and mesh sensitivity in localization problems. Computer Methods in Applied Mechanics and Engineering, 67, 69-85 (1988).

32. Perzyna, P.: The constitutive equations for rate sensitive plastic materials. Quarter of Applied Mathematics, 20, 321-332 (1963).
33. Placidi, L., Barchiesi, E., and Misra, A.: A strain gradient variational approach to damage: a comparison with damage gradient models and numerical results. Mathematics and Mechanics of Complex Systems 6(2), 77-100 (2018).
34. Rice, J. R.: The localization of plastic deformation, Proceedings of the 14th International Congress on Theoretical and Applied Mechanics, Vol. 1, North-Holland Publishing, Amsterdam, Netherlands, 207–220 (1976).
35. Shuttle, D., and I. Smith.: Numerical simulation of shear band formation in soils. International Journal for Numerical and Analytical Methods in Geomechanics 12 (6), 611-626 (1988).
36. Stanier, S. A., Blaber, J., Take, A.W., and White, D. Improved image-based deformation measurement for geotechnical applications. Canadian Geotechnical Journal 53(5), 727-739 (2015).
37. Vardoulakis, I.: Bifurcation analysis of the plane rectilinear deformation on dry sand samples. International Journal of Solids and Structures 17 (11), 1085–1101 (1981).
38. Vardoulakis, I.: Stability and bifurcation of undrained, plane rectilinear deformations on water-saturated granular soils. International Journal for Numerical and Analytical Methods in Geomechanics, 9, 399-414 (1985).
39. Wood, D. M.: Geotechnical modelling (Vol. 1). CRC Press (2004).
40. Yamamuro, J. A. and Lade, P.V.: Static liquefaction of very loose sands. Canadian Geotechnical Journal 34 (6), 905–917 (1997).
41. Yang, Y. and Misra, A.: Micromechanics based second gradient continuum theory for shear band modeling in cohesive granular materials following damage elasticity. International Journal of Solids and Structures 49 (18), 2500-2514 (2012).
42. Zhao, S., Zhao, J., & Lai, Y.: Multiscale modeling of thermo-mechanical responses of granular materials: A hierarchical continuum–discrete coupling approach. Computer Methods in Applied Mechanics and Engineering, 367, 113100 (2020).